Envelope-function-based analysis of the dependence of shot noise on the gate voltage in disordered graphene samples

Paolo Marconcini, * Demetrio Logoteta, and Massimo Macucci
Dipartimento di Ingegneria dell'Informazione, Università di Pisa, Via Caruso 16, I-56122 Pisa, Italy

(Received 4 July 2021; revised 10 October 2021; accepted 12 October 2021; published 25 October 2021)

We perform simulations, by means of an envelope-function-based approach, of shot noise in disordered monolayer graphene devices, as a function of the gate bias voltage. In order to approach the experimental conditions, large graphene samples with characteristic sizes of the order of hundreds of nanometers or microns have been considered. We investigate different device geometries, including back-gated graphene samples with different aspect ratios and a graphene constriction biased by two side gates. We compare our results with available experimental data that were collected by a few authors in an attempt to validate an interesting prediction made by Tworzydło *et al.* [Phys. Rev. Lett. **96**, 246802 (2006)] on the shot noise dependence on carrier density in samples with a large aspect ratio. On the basis of the comparison of our results with the experimental data, we conclude that the effect predicted by Tworzydło *et al.* (resulting from the distribution of the transmission eigenvalues associated with propagation via evanescent modes) has not been observed yet. Finally, we provide some guidelines for the design of experiments aimed at the verification of such an effect.

DOI: 10.1103/PhysRevB.104.155429

I. INTRODUCTION

Graphene, the most recently isolated allotrope of carbon, has been the focus of many research efforts in the last decades. Its lattice structure, consisting of a planar honeycomb lattice of sp^2 hybridized carbon atoms, gives rise to a very peculiar transport behavior and establishes unexpected links with other fields of physics [1–4]. Indeed, its envelope functions satisfy the Dirac-Weyl equation [2,5], which also describes relativistic massless spin-1/2 particles. As a consequence, in graphene, charge carriers experience relativistic-like phenomena [6], such as Klein tunneling and *Zitterbewegung*, at velocities much lower than that of light (the Fermi velocity in graphene is of the order of 10^6 m/s).

Moreover, this one-atom thin and very stable material combines large charge carrier mobility with high thermal conductivity, transparency, mechanical flexibility, and strength. These properties make it very appealing for a broad spectrum of applications, spanning from electronic and optoelectronic devices to electrodes, sensors, energy and gas storage, lubricants, membranes, and coatings [7,8].

Significant theoretical and experimental efforts have focused on the possible application of graphene for the fabrication of electron devices [9]. The absence of an energy gap and the difficulty in introducing it in a controlled and reproducible way have been hampering the usage of graphene for the implementation of field effect devices for digital electronics and this has tempered the enthusiasm about it in the device community. However, different approaches, based for example on the use of alternative device concepts, such as tunnel field-effect transistors, are presently investigated, and applications in other fields of electronics, such as radio-frequency circuits and sensors, have been proposed and are being actively developed. This interest is motivated by the very high mobility of graphene at room temperature and by the possibility to widely tune the transport properties by properly biasing gates located close to it.

In order to increase the signal-to-noise ratio of graphene-based devices, it is important to examine the properties of this material in terms of noise. Several studies have been performed on noise in graphene [10–12] and in particular on shot noise (the noise deriving from the granularity of charge) [13–36]. A commonly used parameter which provides information about the correlation between charge carriers is the Fano factor, i.e., the ratio of the actual shot noise to the full shot noise $2eI$ that would be expected in the case of a Poissonian distribution of the charge carrier crossing events (e is the unit charge, while I is the average current flowing through the device).

In their seminal paper [13], Tworzydło *et al.* showed, with an analytical envelope-function calculation, that the Fano factor for a short and wide ideal graphene strip takes on the maximum value of 1/3, which is reached at the Dirac point. In this condition, charge transport through the strip occurs only via evanescent modes: these modes, tunneling through the short graphene sample (which actually represents a thin potential barrier for charge carriers flowing from the input contact to the output one), make the conductance value nonzero, despite the vanishing density of states in the sample.

Tworzydło *et al.* demonstrated that this relevant result holds as long as there is a very large number of modes propagating in the leads and the aspect ratio of the strip, i.e., the ratio of its width to its length, is around 4 or larger. The value 1/3 is the same as the one characteristic for the Fano factor in disordered conductors [37–39].

*p.marconcini@iet.unipi.it

It was suggested [13] that the reason for this similarity could be the presence of rapid oscillations of the charge carriers, deriving from the interference between the positive- and negative-energy components of the wave packet (this phenomenon, called *Zitterbewegung*, is characteristic of the relativistic quantum dynamics of confined Dirac fermions). These oscillations could give rise to a distribution of transmission eigenvalues analogous to that observed in coherent diffusive conductors, thus resulting in the same value of the Fano factor.

Due to the relevance of the prediction by Tworzydło *et al.*, there have been a few experimental efforts aimed at verifying it by measuring the Fano factor in graphene strips with different aspect ratios and different geometries.

Two papers were published almost simultaneously in 2008, one by DiCarlo *et al.* [17] and the other by Danneau *et al.* [14]. Both papers focused on the measurement of the Fano factor in large aspect ratio graphene samples, obtained by means of exfoliation from highly oriented pyrolytic graphite and deposited on a 300-nm-thick silicon oxide layer grown on top of a heavily doped silicon substrate, which was used as a back gate to control the carrier density in graphene. While DiCarlo *et al.* performed measurements at a temperature of 0.3 K and at a frequency of 1.5 MHz, applying a bias of 300 μV to the device, Danneau *et al.* had a sample temperature of 8.5 K, which required a larger applied bias (40 mV) to obtain a prevalence of shot noise over thermal noise. An increase by about two orders of magnitude of the bias current (resulting from an increase by two orders of magnitude of the bias voltage) implies an increase by two orders of magnitude of the shot noise power spectral density and by four orders of magnitude of the flicker noise power spectral density (which is proportional to the square of the mean current through the device). Thus, in order to be above the flicker noise corner frequency (the frequency at which the flicker noise power spectral density equals the white noise floor, corresponding to the shot noise power spectral density in the case of interest), the measurement frequency had to be increased by about two orders of magnitude, up to the 600–850-MHz range [14,15]. This was done with a very careful approach [15], but the overall accuracy is unavoidably decreased by the increased difficulty in measuring differential resistances and parasitic parameters at higher frequencies.

DiCarlo *et al.* measured, for all but one of their samples (which likely did not consist of monolayer graphene), a Fano factor of about 1/3, which, however, did not exhibit any substantial dependence on the back-gate voltage (and thus on the carrier concentration).

Danneau *et al.* obtained instead quite a different result, observing a variation of the Fano factor as the back-gate voltage was varied, which they attributed to the effect predicted by Tworzydło *et al.*, although the variation occurred over a range of back-gate voltage much larger than the one that could be derived from Ref. [13], as pointed out also by Lewenkopf *et al.* [20].

Lewenkopf *et al.* performed simulations of transport and noise in disordered graphene samples using a tight-binding approach implemented with the recursive Green's function method. The atomistic scale of the approach limited the maximum nanoribbon width that they could simulate to about 20 nm. They considered a disorder formed by a superposition of Gaussian functions and presented their results as a function of a parameter K_0 quantifying the disorder strength [40]. They observed that, as the strength of the disorder is increased, the effect predicted by Tworzydło *et al.* gradually disappears and the Fano factor becomes substantially constant as a function of the charge density, in reasonable agreement (as long as one assumes that the disorder in the measured samples is strong enough) with what has been observed in the experiment by DiCarlo *et al.*, but not with the results by Danneau *et al.*

A large aspect ratio graphene ribbon was more recently investigated by Mostovov [19]. The ribbon was obtained by lithographically defining a constriction in a larger, exfoliated graphene sample. The electrostatic potential in the constriction region (which, being much narrower than the rest of the ribbon, dominates the overall conductance and noise behavior and represents the actual sample under analysis) was controlled by means of two side gates. Measurements were performed at a temperature of about 7.5 K (this is the estimated temperature of the electron gas, which is higher than the cryostat base temperature, 4.2 K, due to Joule heating of the sample) using a cross-correlation technique, with an applied bias of 4 mV and at a frequency of 3.33 MHz. The observed behavior of the Fano factor exhibited a smooth variation as a function of the bias voltage applied to the gates, with a maximum at the Dirac point which was less than 1/3 (approximately 0.24–0.25).

Our purpose in this paper is to overcome the sample size limitation that affected previous simulations, treating devices with a size corresponding to those used in the experiments, i.e., with a length of a few hundred nanometers and a width up to $\approx$1 μm. This has been possible with an envelope-function ($\vec{k}\cdot\vec{p}$) based [5] approach that we have previously developed [41]. While this approach may miss some effect deriving from atomistic-level details, it has proven to be valid in the low energy range as far as potentials varying slowly with respect to the lattice constant are considered [41].

On the basis of the outcome of our simulations, we seek to find a common interpretation of the experimental data, reaching the conclusion that in none of them has the effect predicted by Tworzydło *et al.* been observed yet, and we provide suggestions for experiments aiming at the detection of such an effect, because we believe that it would be important, also from the point of view of basic theory, to finally achieve an experimental confirmation.

The paper is organized as follows. In Sec. II, we describe the simulation model. In Sec. III, we present the results obtained for back-gated samples and compare with the results of the experiments by DiCarlo *et al.* and by Danneau *et al.* In Sec. IV, we report the simulation of the structure experimentally investigated in Ref. [19]. Finally, in Sec. V, we draw our concluding remarks and discuss guidelines for future experiments for the detection of the effect predicted in Ref. [13].

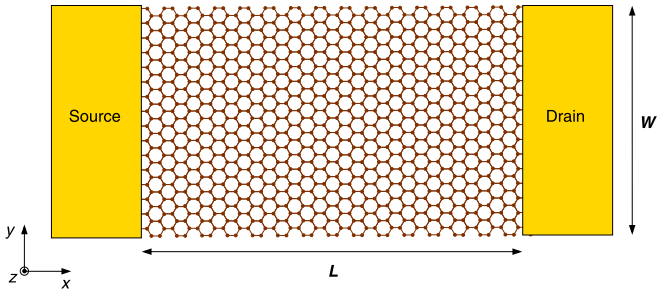

FIG. 1. Sketch of a W-wide and L-long armchair graphene ribbon connected to source and drain contacts.

II. TRANSPORT SIMULATION APPROACH

The numerical simulations that we have performed are based on an envelope-function approach that we have developed [41] for the investigation of transport in graphene samples up to a few microns in size.

In monolayer graphene, the wave function near the Dirac points can be written in terms of four envelope functions $F^{\vec{\alpha}}_{\beta}(\vec{r})$, each one corresponding to one of the two graphene sublattices $\beta = A, B$ and of the two inequivalent Dirac points $\vec{\alpha} = \vec{K}, \vec{K}'$. As previously mentioned, it can be proven that these four functions satisfy the Dirac-Weyl equation [5]:

$$[-i\hbar v_F\,(\partial_x\sigma_x + \partial_y\sigma_y) + U(\vec{r})I]\,\vec{F}^{\vec{K}}(\vec{r}) = E\,\vec{F}^{\vec{K}}(\vec{r}), \quad (1)$$

$$[-i\hbar v_F\,(\partial_x\sigma_x - \partial_y\sigma_y) + U(\vec{r})I]\,\vec{F}^{\vec{K}'}(\vec{r}) = E\,\vec{F}^{\vec{K}'}(\vec{r}), \quad (2)$$

where $\vec{F}^{\vec{\alpha}}(\vec{r}) = [F^{\vec{\alpha}}_A(\vec{r}), F^{\vec{\alpha}}_B(\vec{r})]^T$, $\hbar$ is the reduced Planck constant, v_F is the Fermi velocity of graphene, $\partial_x = \partial/\partial x$, $\partial_y = \partial/\partial y$, the matrices σ are the Pauli matrices, E is the energy of the charge carriers, and U is the potential energy (which depends on the position $\vec{r}$). We consider W-wide armchair graphene ribbons, for which x denotes the transport direction and y denotes the in-plane transversal one (see Fig. 1).

Our transport simulation code [41] relies on a recursive scattering matrix algorithm. The graphene ribbon is first subdivided into a series of cascaded slices (each one parallel to the y direction), sufficiently thin that we can neglect the dependence of the potential energy U on x. Therefore, in each slice the four envelope functions can be factorized as $F(x, y) = e^{ik_x x}\Phi(y)$. By substituting this form into the Dirac-Weyl equation and enforcing Dirichlet boundary conditions on the overall wave function at the edges of the ribbon, we obtain the following system:

$$(\sigma_x f(y) + \sigma_z\partial_y)\,\vec{\varphi}^{\vec{K}}(y) = -\kappa_x\vec{\varphi}^{\vec{K}}(y), \quad (3)$$

$$(\sigma_x f(y) - \sigma_z\partial_y)\,\vec{\varphi}^{\vec{K}'}(y) = -\kappa_x\vec{\varphi}^{\vec{K}'}(y), \quad (4)$$

$$\vec{\varphi}^{\vec{K}}(0) = \vec{\varphi}^{\vec{K}'}(0), \quad (5)$$

$$\vec{\varphi}^{\vec{K}}(W) = e^{i2\tilde{K}W}\vec{\varphi}^{\vec{K}'}(W), \quad (6)$$

where Eqs. (5) and (6) represent the boundary conditions, $\vec{\varphi}^{\vec{K}}(y) = [\Phi^{\vec{K}}_A(y), \Phi^{\vec{K}}_B(y)]^T$, $\vec{\varphi}^{\vec{K}'}(y) = i[\Phi^{\vec{K}'}_A(y), \Phi^{\vec{K}'}_B(y)]^T$, $f(y) = [U(y) - E]/(\hbar v_F)$, $\tilde{K} = K - (\pi/W)\,\mathrm{round}\,[K/(\pi/W)]$, and $K = |\vec{K}|$. By defining, within a suitably enlarged domain $[0, 2W]$, the two-component function [41]

$$\vec{\varphi}(y) = \begin{cases} \vec{\varphi}^{\vec{K}}(y) & \text{for } y \in [0, W] \\ e^{i2\tilde{K}W}\vec{\varphi}^{\vec{K}'}(2W - y) & \text{for } y \in [W, 2W], \end{cases} \quad (7)$$

the system can be rewritten, over $[0, 2W]$, in the following form:

$$[\sigma_z\partial_y + \sigma_x f(W - |W - y|)]\vec{\varphi}(y) = -\kappa_x\vec{\varphi}(y), \quad (8)$$

$$e^{-i2\tilde{K}W}\vec{\varphi}(2W) = \vec{\varphi}(0). \quad (9)$$

Equations (8) and (9) define a differential eigenvalue problem [with periodic boundary conditions on the function $e^{-i\tilde{K}y}\vec{\varphi}(y)$], which can be efficiently solved in the Fourier domain [41,42]. Once the eigenvalues and eigenmodes have been computed in all the slices, we enforce the continuity of the components of the wave function at each interface between adjacent slices. In more detail, we inject a single transport mode at a time into the region straddling the interface and we write the resulting wave function on both sides of the interface as a linear combination of the modes, with unknown transmission and reflection coefficients. Then, we project this set of continuity relations onto a basis set of sine functions, obtaining a system of linear equations with the transmission and reflection coefficients as unknowns. Solving this system, we obtain the scattering matrix of the region which includes the interface. If the width of the ribbon is not uniform (as in the structure of Ref. [19]), the ribbon boundary includes vertical zigzag edges along a portion of each interface between slices of different width. Along such edges, the continuity of the wave function has to be enforced only for one of the two sublattice components. This is achieved by projecting the set of the continuity equations for the other sublattice onto the sine basis of the narrower slice [43]. The overall scattering matrix, and therefore the transmission matrix t of the ribbon, is obtained by recursively composing all the scattering matrices associated to the interfaces between adjacent slices. Finally, the conductance G, the shot noise power spectral density S_I, and the Fano factor F are computed using the formulas due to Landauer and Büttiker [44,45]:

$$G = \frac{2\,e^2}{h}\sum_{n,m}|t_{nm}|^2, \quad S_I = 4\,\frac{e^3}{h}\,|V|\sum_i w_i(1 - w_i), \quad (10)$$

$$F = \frac{S_I}{2\,e\,I} = \frac{\sum_i w_i\,(1 - w_i)}{\sum_i w_i}, \quad (11)$$

where n and m run over the modes propagating in the input and output leads, h is the Planck constant, the w_i's are the eigenvalues of the matrix $t^\dagger t$, V is the average voltage applied between the input and output lead, and $I = GV$ is the average current flowing through the sample. This numerical approach has already been successfully applied to the study of different graphene properties and devices [43,46–49].

The numerator and the denominator of Eq. (11) must be averaged over energy within the transport window before taking their ratio. If the bias voltage is such that $eV \gg kT$, the transport window eV is much wider than the interval over which the Fermi function undergoes an almost unitary variation. Therefore, the Fermi function can be approximated with a step function and the energy averages can be computed

as uniform averages over the transport window eV. For shot noise measurements the condition $eV \gg kT$ is usually verified, in order to make the thermal noise component negligible with respect to the shot noise component.

Let us now discuss the model that we adopt for the description of the contacts and of the potential disorder.

It has been shown [50] that, for large and weakly doped graphene samples, a wide range of contact models leads to analogous transport results. In general, however, it is necessary to guarantee, in every bias condition, a number of propagating modes in the leads sufficiently larger than the one in the sample. This is crucial in order to correctly take into account the contribution of evanescent modes, which do play a dominant role when transport in a large aspect ratio sample at energies close to the Dirac point is considered. Indeed, in Eqs. (10) and (11) the sums run only over the modes propagating in the input and output leads. Let us consider the simple case of a thin and wide clean graphene sample connected between the two leads. If we considered the same potential in the contacts and in the sample, when the Fermi energy coincides with the Dirac point (and thus there is no propagating mode in the sample) Eqs. (10) and (11) would yield a null conductance and shot noise. The correct physical result (with a nonzero conductance and a 1/3 Fano factor, derived from the contribution of the evanescent modes) is recovered using a model which guarantees a sufficient number of propagating modes in the contacts. Accordingly, we have set the (constant) potential energy in the leads at a value sufficiently far from the Fermi energy. In particular, for the bias conditions for which the dominant injected/extracted carriers are electrons (holes) we have chosen a potential energy value in the contacts lower (higher) than the Fermi energy. This ensures that a large number of propagating modes is injected into the sample in all operating conditions, with a symmetric treatment for electrons and holes. Two alternative descriptions have been considered to model the interfaces between the leads and the sample. We have considered either an abrupt, steplike transition or a gradual transition of the potential, with a continuous profile given by the expression $[1 + \tanh(x/x_0)]$. The latter choice, in which the transition takes place over a range of about $6\,x_0$, reduces the reflections at the interfaces.

Such contact models are consistent with physisorbed contacts, in which the interaction energy is very small, and the transfer of charge between the graphene and the metal lowers the graphene Fermi level in the contact area, while the electronic structure of graphene is left substantially unperturbed [51,52]. In the approach by Tworzidło *et al.*, contacts are represented with graphene regions with infinite potential steps, which involve an infinite number of propagating modes, a situation that can be handled in an analytical calculation but not in a numerical one. This is the reason why we have considered a finite potential step, which is also consistent with actual physisorbed contacts [51]. We have also verified that the sensitivity of the results for the Fano factor on the height of the potential step is substantially negligible, as long as a value of at least 100 meV is assumed.

We do not consider chemisorbed contacts in our simulations because they involve a much larger interaction energy, with the hybridization of metal and graphene orbitals, to the extent that the conical K points may be destroyed [51]. Thus the model by Tworzidło is not directly applicable to the case of chemisorbed contacts and physisorbed contacts should be chosen in experiments seeking to validate it.

Potential disorder has been modeled with a superposition of Gaussian functions, each one corresponding to the electrostatic action of one impurity or defect [53]. These Gaussians have been randomly spread all over the graphene sample, with a surface concentration c_{imp}, which represents the surface impurity density of Coulomb scatterers. In particular, the two coordinates on the graphene plane of the centers of the Gaussians have been numerically generated according to random uniform distributions. Each Gaussian is characterized by a half width at half maximum (HWHM), which is assumed to be the same for all the scatterers of a disorder distribution, and by an amplitude which in general differs for the various scatterers and is given by a random number uniformly distributed between $-\delta$ and δ. Therefore, the disorder distribution is characterized by the three parameters c_{imp}, HWHM, and δ. The potential landscape given by the superposition of these Gaussians has a Gaussian autocorrelation function [54]. The relation between the amplitude and variance of this autocorrelation function and the parameters c_{imp}, HWHM, and δ of the distribution of Gaussian scatterers has been reported by Koschny and Schweitzer in Ref. [54]. On the other hand, Adam *et al.* [55,56], using a self-consistent random-phase-approximation method, have found the relation between the parameters which characterize the sample and the amplitude and variance of the resulting autocorrelation function. Combining these two sets of relations [53], it is possible to relate c_{imp}, HWHM, and δ to the actual sample parameters.

III. SIMULATION OF BACK-GATE BIASED GRAPHENE SAMPLES

In order to obtain a preliminary validation of our approach, we have first simulated a structure similar to the one studied by Tworzydło *et al.* [13]. In detail, we have considered a clean 40-nm-long and 200-nm-wide semiconducting graphene ribbon (therefore, with aspect ratio $W/L = 5$) with constant potential energy, contacted with two doped graphene leads of the same width. The potential energy in the two leads is assumed to be equal, in absolute value, to 0.8 eV, while the Fermi energy is set at 0 eV. The effect of the bias applied to the back gate is taken into account through a shift of the potential energy μ in the ribbon. The simulation has been performed for 201 uniformly spaced values of μ between -0.1 and 0.1 eV. By assuming a geometrical capacitance between the back gate and the graphene sheet of ≈ 0.1151 mF/m^2, as in Refs. [14,15,17,18], the interval spanned by μ corresponds to a back-gate voltage window with a width of about 55 V. The mobile charges in the ribbon are holes for $\mu > 0$ and electrons for $\mu < 0$, while for $\mu = 0$ (charge neutrality point) the current is sustained by evanescent modes. The Fano factor as a function of μ, obtained by considering an abrupt potential transition at the lead-sample interfaces (as in the model investigated by Tworzydło *et al.*), is plotted in Fig. 2 with dotted black lines. These results are substantially coincident with those reported by Tworzydło *et al.* in Ref. [13]. The corresponding plot for smooth lead-sample interfaces (with

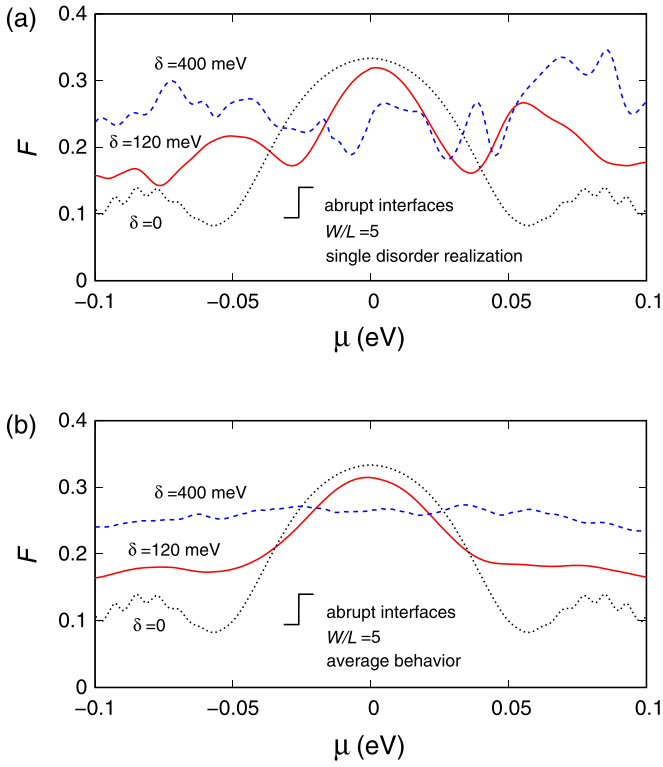

FIG. 2. Fano factor as a function of the potential energy μ in a 40-nm-long and 200-nm-wide armchair ribbon. The Fermi energy is set to 0 eV and abrupt lead-sample interfaces are assumed. The dotted black curves have been obtained in the absence of disorder; the solid red ones have been obtained in the presence of a disorder with $c_{\rm imp} = 5 \times 10^{11}$ cm^{-2}, HWHM $= 5$ nm, and $\delta = 120$ meV; and the dashed blue ones have been obtained in the presence of a disorder with $c_{\rm imp} = 5 \times 10^{11}$ cm^{-2}, HWHM $= 5$ nm, and $\delta = 400$ meV. Panel (a) reports the results obtained for a single impurity distribution, while the results in panel (b) have been obtained by averaging over 48 different impurity distributions.

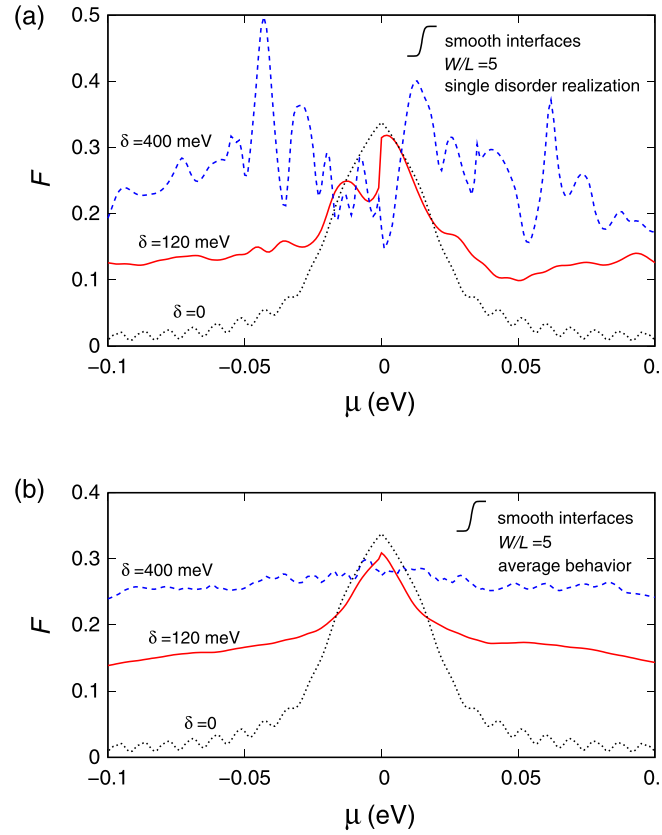

FIG. 3. Same as Fig. 2 for smooth lead-sample interfaces.

$x_0 = 20$ nm) is shown in Fig. 3. This model entails an increase of the effective length of the sample and, as a consequence, the central lobe of the plot narrows with respect to the abrupt interface case (we will observe a similar behavior considering abrupt interfaces and increasing the sample length). Furthermore, the value of the Fano factor for increasing modulus of the potential energy μ drops down to zero instead of reaching an asymptotic value around 0.1, which can be explained as a result of the reduced scattering in the case of a smooth interface.

In order to test to what extent this behavior is preserved in the presence of disorder, we have first repeated our simulations including a random distribution of charged impurities with $c_{\rm imp} = 5 \times 10^{11}$ cm^{-2}, HWHM $= 5$ nm, and $\delta = 120$ meV. According to Adam *et al.*'s relations [55,56], these parameters coherently describe the effect of a distribution of impurities with a concentration of 5×10^{11} cm^{-2} and located at an average distance of 1 nm from the graphene sample. The results are shown with solid red lines in Figs. 2 and 3, for the case of abrupt and smooth contact-sample interfaces, respectively, as a function of the average value μ of the potential energy in the sample. In the panels (a) of these figures we report the results obtained for a single impurity distribution. Then, in order to achieve a representative mean behavior, we have averaged the Fano factor over 48 different impurity distributions; the corresponding results are reported in the panels (b) of Figs. 2 and 3. It can be noticed that the main features observed in the case of a clean graphene sample are preserved, with a main lobe of the shot noise behavior around the Dirac point, although with a maximum value slightly lower than 1/3.

Qualitatively different results are obtained by increasing the maximum disorder amplitude to a much larger value of $\delta = 400$ meV. We report the corresponding results with dashed blue lines in Figs. 2 and 3, for abrupt and smooth contact-sample interfaces, respectively. Also in this case, the panels (a) refer to a single impurity distribution, while the panels (b) refer to the average over 48 different distributions. Here, disorder completely washes out the behavior predicted in Ref. [13] and an average Fano factor almost independent of μ is found.

We have then extended our numerical analysis to graphene samples with lower aspect ratios, but larger sizes. Figure 4 shows the results, averaged over 48 impurity distributions, obtained for a square sample with $W = L = 200$ nm [$W/L = 1$, panel (a)] and for a rectangular sample with $W = 200$ nm and $L = 600$ nm [$W/L = 1/3$, panel (b)]. Abrupt lead-sample interfaces and the same set of δ values previously adopted have been considered (the dotted black, solid red, and dashed blue curves have been obtained for $\delta = 0$, 120, and 400 meV,

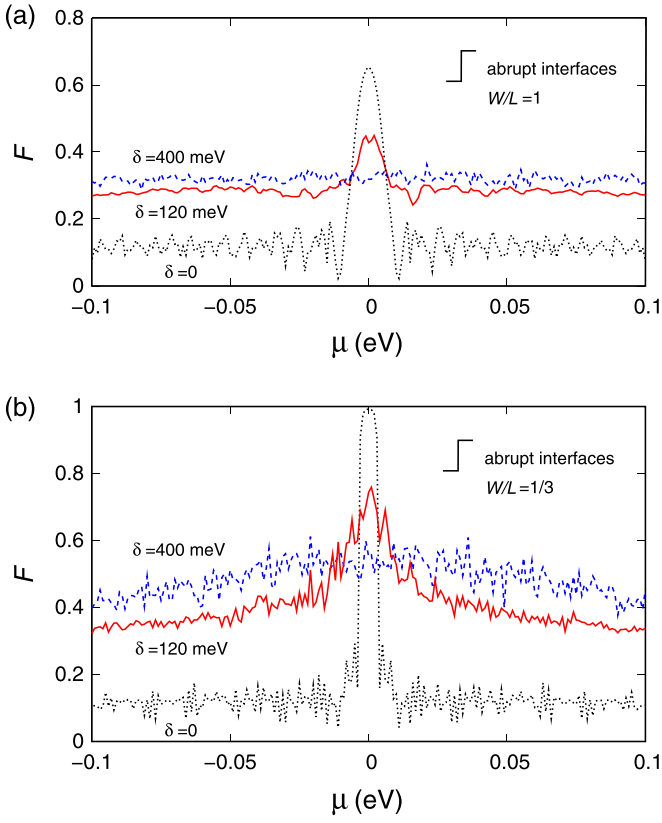

FIG. 4. Fano factor as a function of the potential energy μ in a 200-nm-wide armchair ribbon with a length of 200 nm (a) and 600 nm (b). The Fermi energy is set to 0 eV and abrupt lead-sample interfaces are assumed. The dotted black curves have been obtained in the absence of disorder; the red solid ones have been obtained in the presence of a disorder with $c_{\rm imp} = 5 \times 10^{11}$ cm^{-2}, HWHM = 5 nm, and $\delta = 120$ meV; and the blue dashed ones have been obtained in the presence of a disorder with $c_{\rm imp} = 5 \times 10^{11}$ cm^{-2}, HWHM = 5 nm, and $\delta = 400$ meV. The results have been obtained by averaging over 48 different impurity distributions.

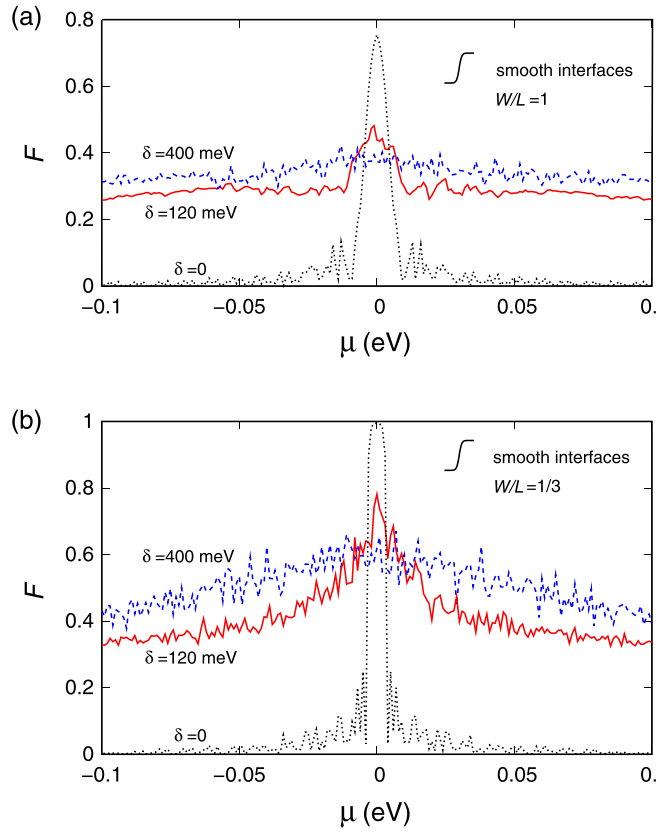

FIG. 5. Same as Fig. 4 for smooth lead-sample interfaces.

respectively). Figure 5 illustrates the corresponding results in the case of smooth lead-sample interfaces.

In Figs. 4 and 5 we observe that, for a given set of disorder parameters, as the length of the sample increases (and therefore the aspect ratio W/L decreases) the value of the Fano factor raises. This is a consequence of the decrease of the transmission probability for increasing ribbon length, and is particularly evident in clean samples close to the Dirac point. It is also consistent with the results in Fig. 2(b) of Ref. [13]. Since in this case transport only occurs via modes which exponentially decay along the device, an increase of the length implies a rapid fall of the transmission to zero. As a consequence, already for $L = 600$ nm the shot noise power spectrum exhibits a Poissonian behavior ($F = 1$). For a given aspect ratio of the ribbon, increasing the disorder strength results in a decrease of the Fano factor close to the Dirac point, while it increases far away from the Dirac point. This is the consequence of the fact that disorder increases the transmission probability close to the Dirac point, by enabling transport via localized states. In contrast, away from the Dirac point, where many transport channels are open, the effect of disorder is to enhance the backscattering, which results in a decrease of the transmission probability and therefore in an increase of F. We also notice that a significant dependence of the results on the sample-lead interface model is only found for clean samples and moderately disordered 40-nm-long samples. Indeed, this dependence disappears as soon as the scattering induced by the disorder becomes dominant with respect to the reflections at the lead-sample interfaces.

We now move on to a semiconducting graphene ribbon with a size analogous to that considered in the experiments ($W = 1$ μm, $L = 200$ nm, and thus $W/L = 5$). We consider abrupt boundary conditions (with a potential step of 0.25 eV) and in Fig. 6 we report the Fano factor as a function of the potential energy μ for no disorder (purple curve); for an intermediate disorder with $c_{\rm imp} = 5 \times 10^{11}$ cm^{-2}, HWHM $= 10$ nm, and $\delta = 50$ meV (green curve); and for a stronger disorder with $c_{\rm imp} = 5 \times 10^{11}$ cm^{-2}, HWHM $= 5$ nm, and $\delta = 120$ meV (red curve). Using the relations obtained by Adam *et al.* [55,56], these values reproduce the electrostatic effect of a distribution of impurities, with concentration $c_{\rm imp}$, at an average distance from graphene equal to 2.15 and 1 nm, respectively.

This result is directly comparable with an experiment performed with a very small applied bias (less than 1 mV, as in the measurements by DiCarlo *et al.*), while we need to average over the transport window for larger values of the applied bias. In particular, if we want to compare with the experiment by Danneau *et al.*, in which a bias of the order of a few tens of millivolts has been applied, we have to average the numerator

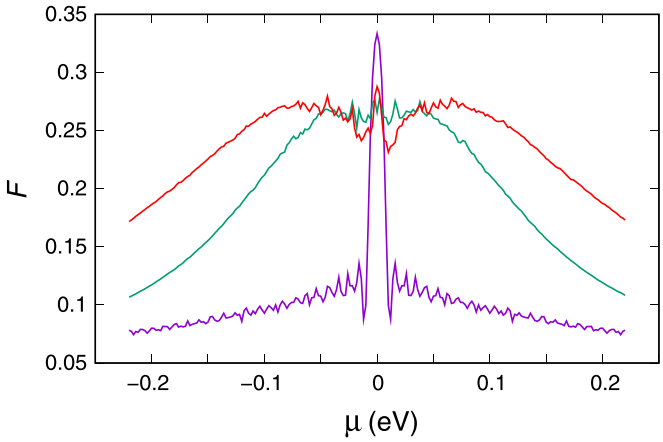

FIG. 6. Fano factor as a function of the potential energy μ for a 200-nm-long and 1000-nm-wide graphene flake ($W/L = 5$) in the absence of disorder (purple line); in the presence of an intermediate disorder with $c_{\rm imp} = 5 \times 10^{11}$ cm^{-2}, HWHM = 10 nm, and $\delta = 50$ meV (green line); and in the presence of a stronger disorder with $c_{\rm imp} = 5 \times 10^{11}$ cm^{-2}, HWHM = 5 nm, and $\delta = 120$ meV (red line).

and the denominator of Eq. (11) over the transport window. In Fig. 7 we report the Fano factor obtained averaging over 30 meV (the results by Danneau *et al.* are actually for a slightly larger applied bias, 40 mV, corresponding to a slightly larger transport window): it is apparent that the narrow feature expected from Tworzydło *et al.*'s theory is almost washed out as a result of the averaging.

This implies that a maximum bias voltage of around 2 mV should be used in an experiment seeking to detect the effect predicted in Ref. [13], at least for samples with a length of the order of a few hundred nanometers.

In order to perform a more direct comparison with experimental data, in Figs. 8 and 9 we plot the results of Figs. 6 and 7 as a function of the applied back-gate voltage. An approximate

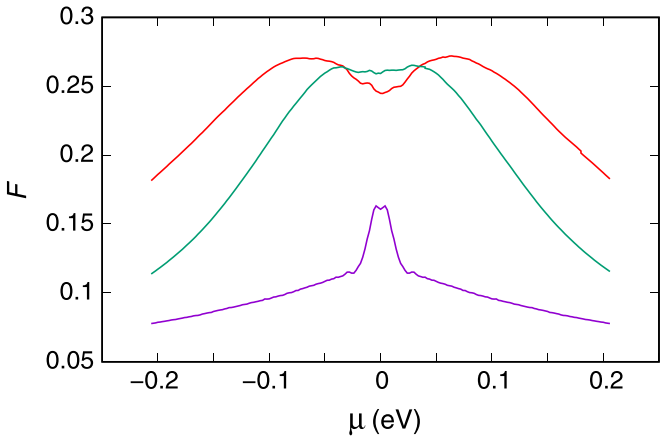

FIG. 7. Fano factor, obtained averaging both noise and conductance over a window of 30 meV before taking their ratio, represented as a function of the potential energy μ for a 200-nm-long and 1000-nm-wide graphene flake ($W/L = 5$) in the absence of disorder (purple line), and in the presence of the intermediate disorder (green line), and of the stronger disorder (red line) specified in Fig. 6.

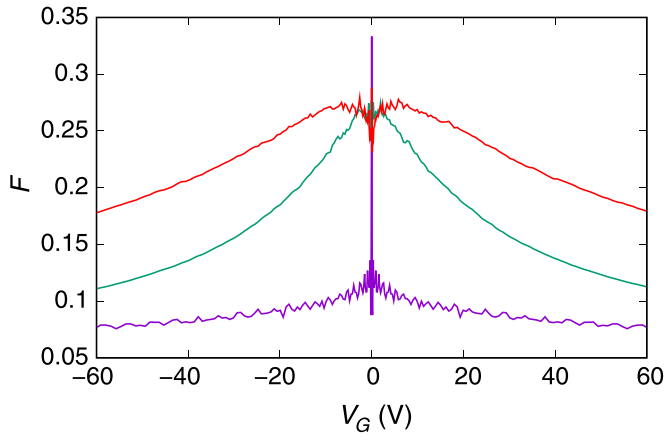

FIG. 8. Fano factor as a function of the applied back-gate voltage V_G for a 200-nm-long and 1000-nm-wide graphene flake ($W/L = 5$) in the absence of disorder (purple line), in the presence of the intermediate disorder (green line), and in the presence of the stronger disorder (red line) specified in Fig. 6.

but reliable relationship between the potential energy μ and the gate voltage V_G can be obtained with an analytical procedure. Under the hypotheses that there is a single back gate, that the graphene sheet is uniform, that the modulus of the potential energy variation $|\Delta\mu|$ is small compared to $|e\Delta V_G|$ (where ΔV_G is the variation of the gate voltage in V), and that the oxide thickness is 300 nm, a very simple expression can be obtained [53,57]:

$$\left|\frac{\Delta\mu}{-e}\right| = \sqrt{\frac{\pi(\hbar v_F)^2 C_G}{e^3}}\sqrt{|\Delta V_G|} = 27.322 \times 10^{-3}\sqrt{|\Delta V_G|}, \tag{12}$$

where $\Delta\mu$ is the variation of the potential energy [and $\Delta\mu/(-e)$ is expressed in V].

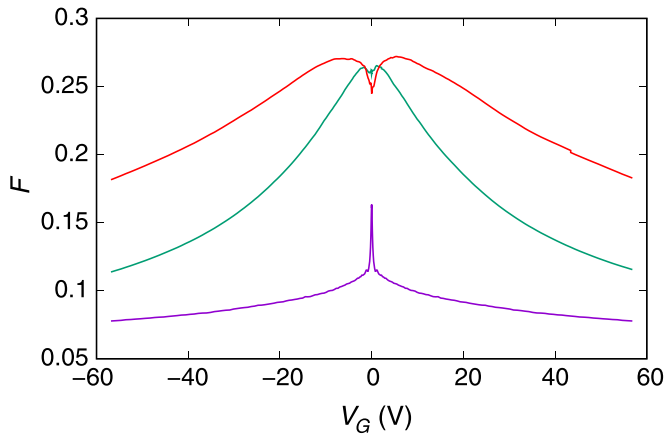

FIG. 9. Fano factor, obtained averaging both noise and conductance over a window of 30 meV before taking their ratio, represented as a function of applied back-gate voltage V_G for a 200-nm-long and 1000-nm-wide graphene flake ($W/L = 5$) in the absence of disorder (purple line), in the presence of the intermediate disorder (green line), and in the presence of the stronger disorder (red line) specified in Fig. 6.

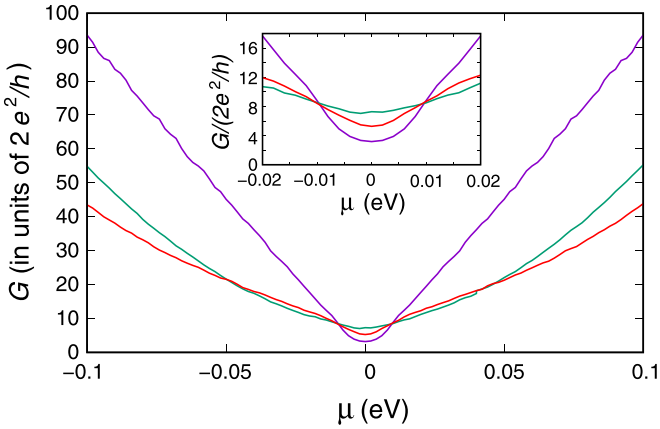

FIG. 10. Conductance as a function of the potential energy μ for a 200-nm-long and 1000-nm-wide graphene flake ($W/L = 5$) in the absence of disorder (purple line), in the presence of the intermediate disorder (green line), and in the presence of the stronger disorder (red line) specified in Fig. 6.

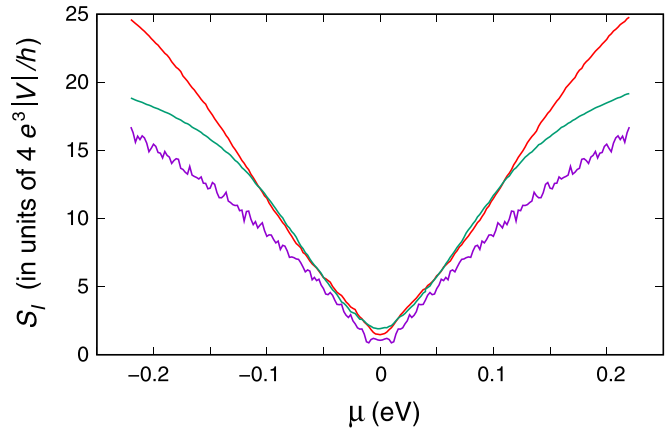

FIG. 11. Shot noise power spectral density as a function of the potential energy μ for a graphene flake 200 nm long and 1000 nm wide ($W/L = 5$) in the absence of disorder (purple line), in the presence of the intermediate disorder (green line), and in the presence of the stronger disorder (red line) considered in Fig. 6.

In Fig. 8 we report the Fano factor as a function of the backgate voltage for the same cases as in Fig. 6: for no disorder (purple curve), for the intermediate disorder (green curve), and for the stronger disorder (red curve). It is apparent that for a realistic device length (in this case 200 nm) the peak resulting from the *Zitterbewegung* effect is extremely narrow, while a much wider peak results from the presence of disorder. Indeed, the expected width of the peak predicted by Tworzydło *et al.* is inversely proportional to the device length L, because in their Eq. (5) the argument of the sine and cosine functions is k_nL, where k_n is the longitudinal wave vector of the associated mode. Thus the peak seen in the experiments by Danneau *et al.*, if attributed to the *Zitterbewegung* effect, would be associated with a much shorter and unrealistic device length, but can instead be simply explained with the action of the disorder. Furthermore, we notice that the Fano factor variation over the considered bias voltage interval decreases (with the exception of a very narrow region around the Dirac point) as the disorder is increased. In Fig. 9 we plot the Fano factor for the very same cases, but after averaging over a transport window of 30 meV. We notice that in the absence of disorder we have an even more suppressed peak, while the peak in the presence of disorder, in particular for the case of the lowest disorder amplitude, has a behavior resembling that observed in the experiments by Danneau *et al.*, although with a smaller maximum value. It is interesting to observe the behavior of the conductance for the same sample with $W/L = 5$: it is plotted in Fig. 10, with the same association between colors and disorder strength: the purple curve is for the situation without disorder, the green curve is for the lower disorder strength, and the red curve is for the higher disorder strength.

Far away from the Dirac point a higher disorder strength leads to a lower conductance, as a result of increased scattering, but around the Dirac point, as it is possible to observe from the inset (containing an enlargement of the region around the origin), we notice that disorder increases conductance, because the irregular fluctuations of the potential create puddles with a potential energy below the Fermi level, among which electrons can tunnel. We point out that the maximum conductance is achieved for the lower disorder strength, since there is a tradeoff between the conductance increase due to the presence of the electron (or hole, depending on the sign of the potential energy shift) puddles and the conductance suppression resulting from the scattering associated with the disordered potential landscape.

A better understanding of the overall behavior of the Fano factor can be obtained from an analysis of the noise behavior, too. In Fig. 11, we report the behavior of the shot noise power spectral density, in units of $4e^3|V|/h$, as a function of the potential energy μ for the same cases as for the previous figures: the purple curve is for the absence of disorder, the green curve is for the intermediate disorder, and the red curve is for the stronger disorder. We see that, while for conductance the fastest growing curve is the one for no disorder, the opposite is true for noise, which means that, as we move away from the Dirac point, the Fano factor, corresponding to the ratio of noise to conductance, will have a larger value for stronger disorder. It will however decay for increasing module of the potential energy, because of the decreasing slope of noise and the increasing slope of conductance. The situation is different close to the Dirac point, because the significant conductance increase in the presence of disorder may lead to a minimum of the Fano factor at the Dirac point, as in the case of the disorder with largest amplitude.

Going back to Fig. 10, we notice that the value of the conductance at the Dirac point in the absence of disorder is approximately $3.25 \times 2e^2/h$, which, dividing by the aspect ratio $W/L = 5$, yields a conductivity $\sigma = 1.3e^2/h$, which is in good agreement with the value of $4e^2/(\pi h) = 1.273e^2/h$ obtained by Tworzydło *et al.*.

A relevant difference between the experimental results by DiCarlo *et al.* and those by Danneau *et al.* is that, in their most significant samples, they obtain quite different conductivities at the Dirac point: while DiCarlo *et al.* report a value of approximately $4e^2/h$ for their sample (A1), the one with the largest aspect ratio ($W/L = 5.71$, with $W = 2$ μm and $L = 0.35$ μm), which is the value usually found in bulk graphene

samples [58], Danneau *et al.* report, for their device with $W/L = 24$, a value of about $4e^2/(\pi h)$, which is consistent with the predictions by Tworzydło *et al.* for large aspect ratios ($W/L \gtrsim 4$) and with the results of our simulations. Measurements performed on graphene samples with several different values of the aspect ratio [59] appear to confirm the theoretically predicted [13] dependence of the minimum conductivity on W/L. More recent numerical models [60] predict a minimum conductance raising to about $4e^2/h$ as disorder is increased, regardless of the aspect ratio of the sample.

Therefore it is possible that the effective aspect ratio of device A1 by DiCarlo *et al.* is actually smaller than expected from the fabrication, and/or that such device is characterized by a very strong disorder. This could also explain the observed independence on carrier density of the measured noise.

Finally, we notice that there are indeed other possible situations leading to a minimum conductivity of $4e^2/(\pi h)$, such as the presence of a relatively low concentration of resonant impurities or vacancies [61,62]. However, in experiments aiming to reproduce the effect predicted in Ref. [13], such a minimum value should derive, as in the analytical calculations by Tworzydło *et al.*, from the transmission of evanescent modes through the potential barrier represented by the high aspect ratio graphene sample between the contacts. Thus, in our simulations we have not included resonant scatterers (which would also be very hard to treat with our envelope-function model), but only the electrostatic scattering induced by charged impurities.

IV. SIMULATION OF A SIDE-GATE BIASED GRAPHENE SAMPLE

More recently, Mostovov [19] sought to achieve an experimental demonstration of the effect predicted by Tworzydło *et al.* with a different type of device: a graphene constriction modulated with side gates.

The representation of their device that we have considered for our simulations is sketched in Fig. 12. It consists of a 1600-nm-wide graphene sample with a 200-nm-long and 500-nm-wide constriction in the center. The size of the constriction was approximately deduced from Fig. 5.11(b) of Ref. [19]. The constriction is biased by means of two gates, deposited around it on the SiO_2 substrate. The gates have been assumed to be 140 nm wide along the x direction and 50 nm thick along z. The distance between them and the graphene sample is set to 30 nm, both in the x and in the y direction. In the previous simulations we have taken into account the effect of the back gate by shifting the potential energy in the sample with respect to the Fermi energy in the contacts. In the present case, however, due to the more complex electrostatics, the potential profile as a function of the gate voltage has been obtained by means of an approximate self-consistent procedure.

A complete numerical self-consistent computation of the electrostatic potential typically requires the solution through a fixed point iterative algorithm of the system of the transport and Poisson equations. At each iteration, the mobile charge density is extracted from the transport results and passed on to the Poisson solver. The latter provides an updated potential profile, to be used in the transport computations at

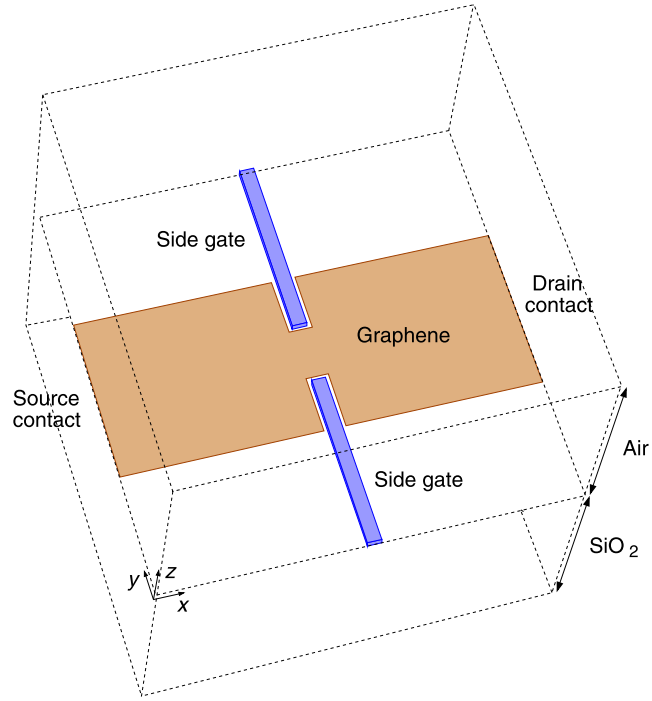

FIG. 12. Geometry of the simulated side-gate structure, modeling the device experimentally studied by Mostovov [19].

the next iteration. The loop ends when the variation of the potential between two consecutive iterations is smaller than a predetermined threshold. Here, we have instead followed the simplified approach of Refs. [46,53], which considerably reduces the computational burden with respect to the previously outlined self-consistent procedure. In detail, the effect in the ribbon of the potential $U(x, y)$, slowly varying in space, can be approximately described as a local, rigid shift in energy of the graphene band structure. As a consequence, the local density of states can be expressed as $\mathrm{LDOS}(E, x, y) = \mathrm{DOS}[E - U(x, y)]$, where $\mathrm{DOS}(E)$ is the density of states in the ribbon. Accordingly, at low temperature, when the Fermi-Dirac distribution can be approximated with a step function, and in quasiequilibrium conditions, the charge density reads

$$\rho(x, y) = e \int_{E_F}^{U(x,y)} \mathrm{LDOS}(E, x, y)\, dE = e \int_{E_F}^{U(x,y)} \mathrm{DOS}[E - U(x, y)]\, dE. \tag{13}$$

$\rho(x, y)$ is positive (hole puddle) for $E_F < U(x, y)$ and negative (electron puddle) for $E_F > U(x, y)$. For relatively large graphene samples, the density of states can be approximated with the one of unconfined graphene [63]: $\mathrm{DOS}(E) = 2|E|/[\pi(\hbar v_F)^2]$. By substituting this expression into Eq. (13), we obtain

$$\rho(x, y) = \mathrm{sign}[U(x, y) - E_F] \frac{e}{\pi(\hbar v_F)^2} [U(x, y) - E_F]^2, \tag{14}$$

which directly yields the charge density as a function of the potential. We assume to know the potential profile $U_0(x, y)$ at

a reference gate voltage V_{G_0}. This reference potential profile $U_0(x, y)$, which actually depends on the unknown properties, such as doping density, of the sample, is chosen in such a way as to obtain the best fit with the experimental results at the corresponding gate voltage V_{G_0}. The corresponding charge density profile $\rho_0(x, y)$ is given by Eq. (14). In order to establish a differential relation between the charge density and the gate bias, we adopt a linearized capacitive model [53,64], which replaces the Poisson equation. Within this approximation, the deviations $\Delta\rho(x, y)$ and $\Delta U(x, y)$ of the charge density and potential from $\rho_0(x, y)$ and $U_0(x, y)$, respectively, induced by a deviation ΔV_G of the gate voltage from the reference value V_{G_0}, satisfy the equation

$$\Delta\rho(x, y) = C_G(x, y)\left(\frac{\Delta U(x, y)}{-e} - \Delta V_G\right), \tag{15}$$

where $C_G(x, y)$ is the (spatially varying) capacitance per unit area between the point (x, y) on the graphene ribbon and the gates. By setting $U = U_0 + \Delta U$ and $\rho = \rho_0 + \Delta\rho$, Eq. (14) can be recast as

$$\rho_0 + C_G\left(\frac{\Delta U}{-e} - \Delta V_G\right) = \mathrm{sign}(U_0 + \Delta U - E_F) \times \frac{e}{\pi(\hbar v_F)^2}(U_0 + \Delta U - E_F)^2, \tag{16}$$

which represents a simple quadratic equation in ΔU. At each point (x, y), the potential energy $U(x, y)$ corresponding to the gate voltage V_G is obtained as $U(x, y) = U_0(x, y) + \Delta U(x, y)$, where $\Delta U(x, y)$ is computed by solving Eq. (16).

This technique requires the knowledge of the electrostatic capacitance between the graphene sample and the double side gate.

In order to compute this quantity, we have numerically solved the Laplace equation in a cubic domain with a 4-μm edge, surrounding the constriction (see Fig. 12). Dirichlet boundary conditions equal to zero and V_G have been enforced on the ribbon and on the side-gate surface, respectively, while Neumann conditions have been enforced on the boundary of the cubic domain. Moreover, the continuity of the normal component of the electric displacement field has been enforced at the interface between the SiO_2 substrate and the air region. According to Gauss's law, the value of the electrostatic potential V close to the graphene sample has then been used to compute the surface charge density $\sigma(x, y)$ on the ribbon:

$$\begin{aligned}\sigma(x, y) &= \epsilon_{\mathrm{air}}(E_z)|_{z=0^+} - \epsilon_{\mathrm{SiO_2}}(E_z)|_{z=0^-} \\ &= \epsilon_{\mathrm{SiO_2}}(\partial V/\partial z)|_{z=0^-} - \epsilon_{\mathrm{air}}(\partial V/\partial z)|_{z=0^+}\end{aligned} \tag{17}$$

(z is null on the graphene sample and increases in the upward direction, ϵ_{air} is the permittivity of air, and $\epsilon_{\mathrm{SiO_2}}$ is that of silicon oxide). The capacitance $C_G(x, y)$ per unit area which exists between each point [with coordinates (x, y)] of the graphene sample and the double side gate is obtained dividing the charge density $\sigma(x, y)$ by the potential difference $-V_G$ between the graphene sample and the double side gate:

$$C_G(x, y) = -\sigma(x, y)/V_G. \tag{18}$$

The transport simulation domain is sketched in Fig. 13(a). In Fig. 13(b) we show a map of $C_G(x, y)$ over this domain.

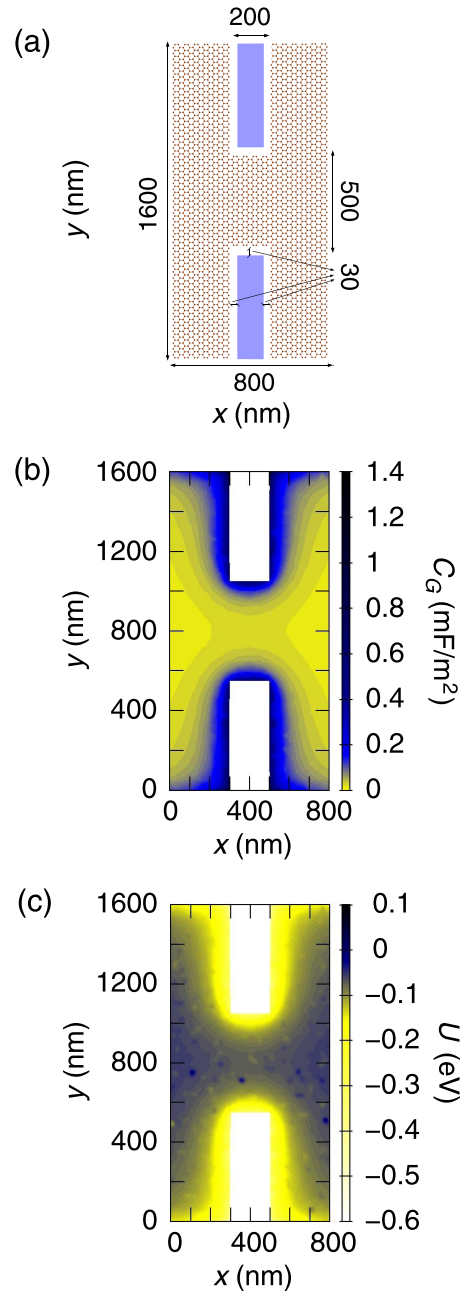

FIG. 13. (a) Sketch of the region of the side-gate biased graphene sample for which transport simulations have been performed. The represented hexagonal lattice is not to scale. (b) Map [in the region of the device sketched in panel (a)] of the capacitance per unit area $C_G(x, y)$ between the double side gate and the point (x, y) of the graphene sample, as a function of the coordinates x and y of the point. (c) Map [in the region of the device sketched in panel (a)] of the graphene potential energy profile $U(x, y)$ obtained for $V_G = 90$ V.

The left and right leads have been modeled as 1600-nm-wide doped graphene regions, with a potential energy equal, in absolute value, to 0.2 eV. A smooth profile (with $x_0 = 25$ nm) is included to connect the potential energy profile in the leads with the one in the sample. The reference voltage has been chosen as $V_{G_0} = 60$ V, i.e., the value at which the measured

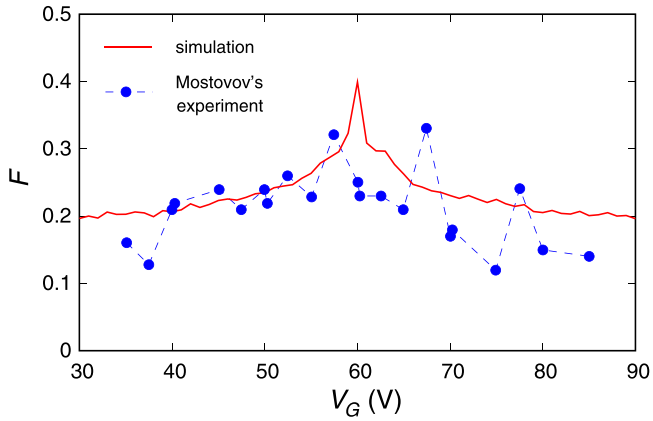

FIG. 14. Fano factor F as a function of the gate voltage V_G. Our numerical results are shown with a red solid line, while the experimental results of Mostovov, extracted from Fig. 9.7 of Ref. [19], are reported with blue dots.

resistance of the device is maximum, and therefore corresponds to the condition in which the lead Fermi energy E_F is aligned with the Dirac point in the sample. The corresponding potential profile U_0 has been obtained by adding the effect of a random impurity distribution to a smooth potential with average value E_F inside the constriction. The best fit with the experimental measurements has been obtained by assuming for the impurity distribution $c_{\rm imp} = 5 \times 10^{10}$ cm^{-2}, $\delta =$ 40 meV, and HWHM $= 17$ nm. According to Refs. [55,56], this set of parameters describes a realistic distribution of charged impurities with concentration 5×10^{10} cm^{-2} and located at an average distance of 1 nm from the sample. As an example, in Fig. 13(c) we show a map over the transport simulation domain of the potential energy obtained for $V_G = 90$ V. In Fig. 14, the result of our simulation for the Fano factor (red line), reported as a function of the gate bias, is compared with the experimental data extracted from Fig. 9.7 of Ref. [19]. The simulation results appear to provide a reasonable fit to the experimental data. It is apparent that also in this case the variation of the Fano factor visible in the simulation results occurs over a gate bias voltage range far larger than that which would be characteristic of the effect predicted by Tworzydło *et al.*, and therefore can be attributed to an effect analogous to the one we have discussed for the back-gated disordered sample with $W = 1$ μm and $L = 200$ nm. Such an effect is thus of a general nature in samples with a relatively low degree of disorder and appears to be independent of the specific details of the sample geometry and electrostatics.

V. CONCLUSIONS

We have performed envelope-function-based simulations of shot noise in disordered gate-biased graphene samples with the aim of interpreting published measurement results aiming at the experimental verification of the interesting effect on the Fano factor of large aspect ratio graphene samples predicted in Ref. [13]. Contrary to existing atomistic simulations, our continuum approach has allowed us to study relatively large graphene structures, with a size of the order of microns, comparable to that of most of the actually measured samples. To provide a physical picture as comprehensive as possible, we have simulated graphene samples with different geometries, levels of disorder, contact models, and gate arrangements. Our conclusion is that in none of the experiments that we have reviewed was the effect predicted by Tworzydło *et al.* actually detected, because either no peak of the Fano factor was observed as a function of the gate bias voltage or the observed peak had a width inconsistent by orders of magnitude with that predicted by Tworzydło *et al.* and should therefore be attributed to the interplay of disorder and carrier density.

On the basis of our results, further experiments seeking to confirm the effect of Ref. [13] should follow a few guidelines.

(a) The applied bias voltage should be as small as possible, preferably less than 1 mV (in order to prevent averaging over the transport window, which would significantly suppress the expected peak, at least for a reasonable length of the sample, of the order of a few hundred nanometers), and therefore the sample temperature should be below 1 K or less (to achieve a shot noise power spectral density at least an order of magnitude larger that that of thermal noise).

(b) The disorder in the graphene sample should be as small as possible, because, at least for samples of a realistic size, disorder leads to a significant variation of the dependence of the Fano factor on gate voltage or even to a complete suppression of the sought-after effect: it would thus be advisable to use suspended samples, which are not affected by the disorder in the substrate.

(c) Contacts should be physisorbed, because, as discussed in Sec. II, only physisorbed contacts are fully consistent with the model in Ref. [13], and, in addition, they should exhibit the least possible resistance, unless the device geometry allows four-probe measurements.

(d) The sample conductivity at the Dirac point should be equal to $4e^2/(\pi h)$, consistent with the results in Ref. [13] (although this by itself is not a guarantee that the same conditions as those considered by Tworzydło *et al.* are present, because, as previously mentioned, such a minimum conductivity could also be the result, for example, of resonant impurities).

(e) Compatibly with the flicker noise level, measurements should be performed at a frequency as low as possible, because correction and calibration procedures become more complex and more susceptible to errors as the frequency is increased.

A carefully designed experiment following the above guidelines should allow detection of the peculiar behavior of shot noise predicted by Tworzydło *et al.*, as long as the parasitic effects (in particular those due to disorder) are kept under control.

ACKNOWLEDGMENTS

This work was partially supported by the Italian Ministry of Education and Research (MIUR) in the framework of the "CrossLab" project (Departments of Excellence) and by the University of Pisa in the framework of the PRA 2020-2021 project "Quantum computing, technologies and applications."

[1] A. K. Geim and K. S. Novoselov, The rise of graphene, Nat. Mater. **6**, 183 (2007).

[2] A. H. Castro Neto, F. Guinea, N. M. R. Peres, K. S. Novoselov, and A. K. Geim, The electronic properties of graphene, Rev. Mod. Phys. **81**, 109 (2009).

[3] M. I. Katsnelson, *Graphene: Carbon in Two Dimensions* (Cambridge University, Cambridge, England, 2012).

[4] T. Enoki and T. Ando, *Physics and Chemistry of Graphene: Graphene to Nanographene* (CRC, Boca Raton, FL, 2014).

[5] P. Marconcini and M. Macucci, The k·p method and its application to graphene, carbon nanotubes and graphene nanoribbons: The Dirac equation, Riv. Nuovo Cim. **34**, 489 (2011).

[6] M. I. Katsnelson and K. S. Novoselov, Graphene: New bridge between condensed matter physics and quantum electrodynamics, Solid State Commun. **143**, 3 (2007).

[7] K. S. Novoselov, V. I. Fal'ko, L. Colombo, P. R. Gellert, M. G. Schwab, and K. Kim, A roadmap for graphene, Nature (London) **490**, 192 (2012).

[8] M. Sharon and M. Sharon, *Graphene: An Introduction to the Fundamentals and Industrial Applications* (Wiley, New York, 2015).

[9] F. Schwierz, Graphene transistors: Status, prospects, and problems, Proc. IEEE **101**, 1567 (2013).

[10] A. A. Balandin, Low-frequency 1/f noise in graphene devices, Nat. Nanotechnol. **8**, 549 (2013).

[11] B. Pellegrini, P. Marconcini, M. Macucci, G. Fiori, and G. Basso, Carrier density dependence of $1/f$ noise in graphene explained as a result of the interplay between band-structure and inhomogeneities, J. Stat. Mech. (2016) 054017.

[12] M. Macucci and P. Marconcini, Theoretical comparison between the flicker noise behavior of graphene and of ordinary semiconductors, J. Sensors **2020**, 2850268 (2020).

[13] J. Tworzydło, B. Trauzettel, M. Titov, A. Rycerz, and C. W. J. Beenakker, Sub-Poissonian Shot Noise in Graphene, Phys. Rev. Lett. **96**, 246802 (2006).

[14] R. Danneau, F. Wu, M. F. Craciun, S. Russo, M. Y. Tomi, J. Salmilehto, A. F. Morpurgo, and P. J. Hakonen, Shot Noise in Ballistic Graphene, Phys. Rev. Lett. **100**, 196802 (2008).

[15] R. Danneau, F. Wu, M. F. Craciun, S. Russo, M. Y. Tomi, J. Salmilehto, A. F. Morpurgo, and P. J. Hakonen, Evanescent wave transport and shot noise in graphene: Ballistic regime and effect of disorder, J. Low Temp. Phys. **153**, 374 (2008).

[16] R. Danneau, F. Wu, M. F. Craciun, S. Russo, M. Y. Tomi, J. Salmilehto, A. F. Morpurgo, and P. J. Hakonena, Shot noise measurements in graphene, Solid State Commun. **149**, 1050 (2009).

[17] L. DiCarlo, J. R. Williams, Y. Zhang, D. T. McClure, and C. M. Marcus, Shot Noise in Graphene, Phys. Rev. Lett. **100**, 156801 (2008).

[18] Z. B. Tan, A. Puska, T. Nieminen, F. Duerr, C. Gould, L. W. Molenkamp, B. Trauzettel, and P. J. Hakonen, Shot noise in lithographically patterned graphene nanoribbons, Phys. Rev. B **88**, 245415 (2013).

[19] A. Mostovov, Quantum shot noise in graphene, Ph.D. thesis, Université Pierre et Marie Curie–Paris VI, 2014, https://hal.archives-ouvertes.fr/tel-01023003/document.

[20] C. H. Lewenkopf, E. R. Mucciolo, and A. H. Castro Neto, Numerical studies of conductivity and Fano factor in disordered graphene, Phys. Rev. B **77**, 081410(R) (2008).

[21] P. San-Jose, E. Prada, and D. S. Golubev, Universal scaling of current fluctuations in disordered graphene, Phys. Rev. B **76**, 195445 (2007).

[22] G. J. Xu, Y. M. Zhu, B. H. Wu, X. G. Xu, and J. C. Cao, Impact of induced bandgaps on sub-Poissonian shot noise in graphene armchair-edge nanoribbons, J. Appl. Phys. **112**, 073716 (2012).

[23] J.-H. Yuan, Z. Cheng, J.-J. Zhang, Q.-J. Zeng, and J.-P. Zhang, Voltage-driven electronic transport and shot noise in armchair graphene nanoribbons, Phys. Lett. A **375**, 2670 (2011).

[24] V. A. Gopar, Shot noise fluctuations in disordered graphene nanoribbons near the Dirac point, Physica E **77**, 23 (2016).

[25] S. Das Sarma, S. Adam, E. H. Hwang, and E. Rossi, Electronic transport in two-dimensional graphene, Rev. Mod. Phys. **83**, 407 (2011).

[26] E. B. Sonin, Charge transport and shot noise in a ballistic graphene sheet, Phys. Rev. B **77**, 233408 (2008).

[27] A. Schuessler, P. M. Ostrovsky, I. V. Gornyi, and A. D. Mirlin, Analytic theory of ballistic transport in disordered graphene, Phys. Rev. B **79**, 075405 (2009).

[28] A. Schuessler, P. M. Ostrovsky, I. V. Gornyi, and A. D. Mirlin, Full counting statistics in disordered graphene at the Dirac point: From ballistics to diffusion, Phys. Rev. B **82**, 085419 (2010).

[29] A. Golub and B. Horovitz, Shot noise in graphene with long-range Coulomb interaction and local Fermi distribution, Phys. Rev. B **81**, 245424 (2010).

[30] M. F. Borunda, H. Hennig, and E. J. Heller, Ballistic versus diffusive transport in graphene, Phys. Rev. B **88**, 125415 (2013).

[31] A. D. Wiener and M. Kindermann, Effects of the contacts on shot noise in graphene nanoribbons, Phys. Rev. B **90**, 035409 (2014).

[32] A. Laitinen, G. S. Paraoanu, M. Oksanen, M. F. Craciun, S. Russo, E. Sonin, and P. Hakonen, Contact doping, Klein tunneling, and asymmetry of shot noise in suspended graphene, Phys. Rev. B **93**, 115413 (2016).

[33] J. Cayssol, B. Huard, and D. Goldhaber-Gordon, Contact resistance and shot noise in graphene transistors, Phys. Rev. B **79**, 075428 (2009).

[34] R. Danneau, F. Wu, M. Y. Tomi, J. B. Oostinga, A. F. Morpurgo, and P. J. Hakonen, Shot noise suppression and hopping conduction in graphene nanoribbons, Phys. Rev. B **82**, 161405(R) (2010).

[35] E. B. Sonin, Effect of Klein tunneling on conductance and shot noise in ballistic graphene, Phys. Rev. B **79**, 195438 (2009).

[36] A. Rycerz, P. Recher, and M. Wimmer, Conformal mapping and shot noise in graphene, Phys. Rev. B **80**, 125417 (2009).

[37] M. Henny, S. Oberholzer, C. Strunk, and C. Schönenberger, 1/3-shot-noise suppression in diffusive nanowires, Phys. Rev. B **59**, 2871 (1999).

[38] F. Liefrink, J. I. Dijkhuis, M. J. M. de Jong, L. W. Molenkamp, and H. van Houten, Experimental study of reduced shot noise in a diffusive mesoscopic conductor, Phys. Rev. B **49**, 14066 (1994).

[39] C. W. J. Beenakker and M. Büttiker, Suppression of shot noise in metallic diffusive conductors, Phys. Rev. B **46**, 1889(R) (1992).

[40] A. Rycerz, J. Tworzydło, and C. W. J. Beenakker, Anomalously large conductance fluctuations in weakly disordered graphene, Europhys. Lett. **79**, 57003 (2007).

[41] D. Logoteta, P. Marconcini, C. Bonati, M. Fagotti, and M. Macucci, High-performance solution of the transport problem in a graphene armchair structure with a generic potential, Phys. Rev. E **89**, 063309 (2014).

[42] P. Marconcini, D. Logoteta, and M. Macucci, Sinc-based method for an efficient solution in the direct space of quantum wave equations with periodic boundary conditions, J. Appl. Phys. **114**, 173707 (2013).

[43] P. Marconcini and M. Macucci, Symmetry-dependent transport behavior of graphene double dots, J. Appl. Phys. **114**, 163708 (2013).

[44] M. Büttiker, Y. Imry, R. Landauer, and S. Pinhas, Generalized many-channel conductance formula with application to small rings, Phys. Rev. B **31**, 6207 (1985).

[45] M. Büttiker, Scattering Theory of Thermal and Excess Noise in Open Conductors, Phys. Rev. Lett. **65**, 2901 (1990).

[46] E. D. Herbschleb, R. K. Puddy, P. Marconcini, J. P. Griffiths, G. A. C. Jones, M. Macucci, C. G. Smith, and M. R. Connolly, Direct imaging of coherent quantum transport in graphene p-n-p junctions, Phys. Rev. B **92**, 125414 (2015).

[47] P. Marconcini and M. Macucci, Envelope-function-based transport simulation of a graphene ribbon with an antidot lattice, IEEE Trans. Nanotechnol. **16**, 534 (2017).

[48] P. Marconcini and M. Macucci, Effects of a magnetic field on the transport and noise properties of a graphene ribbon with antidots, Nanomaterials **10**, 2098 (2020).

[49] P. Marconcini and M. Macucci, Geometry-dependent conductance and noise behavior of a graphene ribbon with a series of randomly spaced potential barriers, J. Appl. Phys. **125**, 244302 (2019).

[50] H. Schomerus, Effective contact model for transport through weakly-doped graphene, Phys. Rev. B **76**, 045433 (2007).

[51] P. A. Khomyakov, G. Giovannetti, P. C. Rusu, G. Brocks, J. van den Brink, and P. J. Kelly, First-principles study of the interaction and charge transfer between graphene and metals, Phys. Rev. B **79**, 195425 (2009).

[52] F. Giubileo and A. Di Bartolomeo, The role of contact resistance in graphene field-effect devices, Prog. Surf. Sci. **92**, 143 (2017).

[53] P. Marconcini and M. Macucci, Approximate calculation of the potential profile in a graphene-based device, IET Circ. Device. Syst. **9**, 30 (2015).

[54] Th. Koschny and L. Schweitzer, Levitation of the quantum Hall extended states in the $B \to 0$ limit, Phys. Rev. B **70**, 165301 (2004).

[55] S. Adam, S. Cho, M. S. Fuhrer, and S. Das Sarma, Density Inhomogeneity Driven Percolation Metal-Insulator Transition and Dimensional Crossover in Graphene Nanoribbons, Phys. Rev. Lett. **101**, 046404 (2008).

[56] S. Adam, Graphene carrier transport theory, in *Graphene Nanoelectronics. Metrology, Synthesis, Properties and Applications*, edited by H. Raza (Springer-Verlag, Berlin, 2012), Chap. 12.

[57] R. V. Gorbachev, A. S. Mayorov, A. K. Savchenko, D. W. Horsell, and F. Guinea, Conductance of p-n-p graphene structures with "air-bridge" top gates, Nano Lett. **8**, 1995 (2008).

[58] K. S. Novoselov, A. K. Geim, S. V. Morozov, D. Jiang, M. I. Katsnelson, I. V. Grigorieva, S. V. Dubonos, and A. A. Firsov, Two-dimensional gas of massless Dirac fermions in graphene, Nature (London) **438**, 197 (2005).

[59] F. Miao, S. Wijeratne, Y. Zhang, U. C. Coskun, W. Bao, and C. N. Lau, Phase-coherent transport in graphene quantum billiards, Science **317**, 1530 (2007).

[60] R. N. Sajjad, F. Tseng, K. M. Masum Habib, and A. W Ghosh, Quantum transport at the Dirac point: Mapping out the minimum conductivity from pristine to disordered graphene, Phys. Rev. B **92**, 205408 (2015).

[61] T. O. Wehling, S. Yuan, A. I. Lichtenstein, A. K. Geim, and M. I. Katsnelson, Resonant Scattering by Realistic Impurities in Graphene, Phys. Rev. Lett. **105**, 056802 (2010).

[62] S. Yuan, H. De Raedt, and M. I. Katsnelson, Modeling electronic structure and transport properties of graphene with resonant scattering centers, Phys. Rev. B **82**, 115448 (2010).

[63] P. R. Wallace, The band theory of graphite, Phys. Rev. **71**, 622 (1947).

[64] M. R. Connolly, R. K. Puddy, D. Logoteta, P. Marconcini, M. Roy, J. P. Griffiths, G. A. C. Jones, P. A. Maksym, M. Macucci, and C. G. Smith, Unraveling quantum Hall breakdown in bilayer graphene with scanning gate microscopy, Nano Lett. **12**, 5448 (2012).